

# Modification and Adaptation of SEBAL-Based LSE Estimation Method for LDCM Data: Fars Province, Iran

Hassan Emami<sup>1</sup>, Abdolreza Safari<sup>2</sup>, and Barat Mojaradi<sup>3</sup>

1-Assistant Professor, Department of Geomatics, University of Tabriz

2-Professor, Department of Surveying and Geomatics, University of Tehran

3-Assistant Professor, Department of Geomatics, Iran University of Science and Technology

<sup>1</sup> h\_emami@tabrizu.ac.ir, <sup>2</sup> asafari@ut.ac.ir, <sup>3</sup> mojaradi@iust.ac.ir

**Abstract**— Land Surface Emissivity (LSE) is an important intrinsic property of materials that is variable through physical parameters and it is dependent on the Spectral Response Function (SRF) and the effective wavelength of the channel. Surface Energy Balance Algorithm for Land (SEBAL) is one of the most widely applied models, which is comprised of twenty-five sub-models that calculate different surface variables such as LSE and LST. This algorithm used within 3-14  $\mu\text{m}$  and 8-14  $\mu\text{m}$  spectral domain as a broadband and narrowband, respectively. The 8-14  $\mu\text{m}$  spectral domain in the Landsat-8 (known as Landsat Data Continuity Mission, LDCM) divided to two very narrowband thermal infrared bands (TIR) (10.60 - 11.19  $\mu\text{m}$ ) and (11.50 - 12.51  $\mu\text{m}$ ) spectral ranges. This study investigates the effects of SRF and effective wavelength of two LDCM TIR bands on SEBAL-based LSE estimation method. The effectiveness of the modification proposed method,  $M_{LSE}SEBAL$ , is empirically tested over one scene of LDCM data and the obtained LSEs by initial and modified methods were compared to the LSE product of the ASTER as a reference by image-based and class-based cross-validation. The results showed that the  $M_{LSE}SEBAL$  demonstrated better performance rather than initial SEBAL LSE estimation method in term of RMSE. Indeed, the RMSE values of LSE obtained by initial and modification SEBAL are 1.37% (for b10) and 1.12% (for b 11) which, lead to 1.16 K and 1.03 K errors and 0.46% (for b10) and 0.39% (for b 11) which lead to 0.39 K and 0.36 K errors in the LST retrieval in the first scene, respectively. Similarly, for the second scene, the RMSE values are 0.69% (for b10) and 0.65% (for b 11) which lead to 0.6 K and 0.58 K errors and 0.46% (for b10) and 0.43% (for b 11) which lead to 0.40 K and 0.39 K errors, respectively. The achieved LSEs of initial SEBAL and modification methods showed that if there is little difference in the effective wavelength between broadband and narrowband, the LSE estimation is almost identical to the non-vegetated area and there is no significant difference, while it is non-negligible in the vegetated area. Moreover, the  $M_{LSE}SEBAL$  compared to three common LSE estimation

methods and the results showed that there are a consistent result among the compared and modified SEBAL-based LSE estimation methods.

**Keywords**—ASTER, Land surface emissivity, LDCM, Modification SEBAL, SEBAL.

## I. INTRODUCTION

Land surface emissivity (LSE) is defined as the "emitting ability" of a natural material, compared to that of an ideal blackbody at the same temperature [1]. Emissivity is a measure of the inherent efficiency of the surface to convert heat energy into radiant energy. There are several definitions of the emissivity, such as the, e-emissivity, r-emissivity and the apparent emissivity [2]. The e-emissivity is defined as the ratio of the total radiation of a natural object surface to the blackbody radiation by assuming that there is an identical temperature distribution with heterogeneous pixels[2]. [3] pointed out that heterogeneous gray surfaces, do not behave as gray of surfaces. To handle this problem, apparent emissivity was proposed to keep the Planck's function unchanged. According to the Kirchhoff's law, [4] defined the r-emissivity from the hemispherical directional reflectivity. The r-emissivity definition is based on the Kirchhoff's law and applicable for heterogeneous flat surfaces. Since, the r-emissivity is measured from space; it is used for LSE retrieval from space-based measurements. Because different composition of surface objects is always combined in one single pixel, the emissivity is complicated to estimate. Satellite-based emissivity estimates depend

largely on the composition, roughness and other physical parameters of the surface, such as its moisture content [5]. LSE is not only a basic parameter for land surface temperature (LST) retrieval, but also a vital parameter to measure the thermal infrared radiation of objects [6]. LSE provides useful information for geological and environmental studies, mineral mapping and it is one of the important input parameters for climate, hydrological, ecological and biological models [7, 8]. Several methods exist to estimate spectral emissivity from satellite data, which apply the Visible and Near-Infrared (VNIR) or Thermal Infrared (TIR) spectral regions or both of them [2]. According to the way by which the LSE is determined along with LST, the emissivity estimation methods of optical remote sensing data can be categorized into three distinct types [2].

The first group is a stepwise retrieval method that determines the LSE and the LST separately. Representative methods of this group include the NDVI Based Emissivity Method (NBEM) [9, 10], Surface Energy Balance Algorithm for Land (SEBAL) [11], the Classification-Based Emissivity Method (CBEM) [12, 13], and so forth. The second group of algorithms retrieve simultaneous both LSE and LST with known atmospheric information from at-surface radiance, based on some assumptions or constraints. The representative methods of this group consist of the physics-based day/night operational method [14], normalized emissivity method (NEM) [15], adjusted normalized emissivity method (ANEM) [16, 17], surface reflectance signature classification (SRSC) [18], the reference channel method (RCM) [19], temperature emissivity separation (TES) method [20], gray body emissivity method (GBEM) [21], and so on. The third group simultaneously retrieves the atmospheric profiles along with both LST and LSE. The representatives of this group are the artificial neural network (ANN) method [22] and the two-step physical retrieval method [23] which are mostly used for thermal hyperspectral imaging.

As described, various LSE estimation methods have been proposed with the same aims and conditions of various applications, benefits, and limitations [2]. The emissivity of natural surfaces may vary significantly due to differences in soil structure, soil composition, organic matter, moisture content and differences in vegetation cover characteristics. LSE is also a function of the wave bandwidth [24]. Broadband thermal emissivity has been shown to vary considerably from narrowband values for the same surface [25]. Broadband emissivity, especially in the 8-14  $\mu\text{m}$  region, is also susceptible to the effects of atmospheric water vapour [10]. Also, the dynamic range of emissivities of contrasting surfaces is greater in the broadband than in the narrowband, and may result in a greater potential for error in surface temperature calculations [24]. Moreover, a few studies have shown that an error of 1 % in the LSE can lead to an error in the LST ranging from 1 K to 2 K in LST using single channel (SC) algorithm around 10 microns [2]. Thus, a small

improvement in LSE can influence LST remarkably. The studies by [26] showed that the use of the broadband emissivity in one channel instead of the narrowband emissivity may result in large errors on the calculated surface parameters. On the other hand, there are few spectral measurements available beyond 14.0  $\mu\text{m}$  for natural objects because of the limitation of the measured instruments and the strong atmospheric absorption in the longwave TIR region [26]. In addition, there are also very narrow spectral channels in the atmospheric windows for satellite sensors. Now the question arises: which spectral domain's emissivity can best representative of the narrowband and broadband emissivity in the completely electromagnetic region for the calculation of the Earth emitted radiant flux and surface parameters. The splitting of the electromagnetic spectra into several spectral domains and computing the contribution of each spectral domain to the overall value of the Earth emitted radiant flux can be considered as a suitable approach [27].

SEBAL is one of the most widely applied remotely sensed surface energy balance models which is comprised of twenty-five computational sub-models that calculate surface variables such as evapotranspiration (ET), LSE, LST and other energy exchange at the earth's surface [28]. The broadband surface emissivity is an important parameter for estimating the longwave surface energy in SEBAL methodology. The broadband emissivity can vary significantly, because the spectral emissivity ranges from 0.7 to 1.0 for bare soils and rocks in the 8–12  $\mu\text{m}$  range. Two surface emissivities are used in the SEBAL algorithm. The first is an emissivity representing the surface behavior for thermal emission expressed as  $\epsilon_{\text{NB}}$ . The second is an emissivity representing the surface behavior for thermal emission in the broad thermal spectrum (6 to 14  $\mu\text{m}$ ), expressed as  $\epsilon_0$ .  $\epsilon_{\text{NB}}$  is used in the calculation of LST and  $\epsilon_0$  is used later on to calculate total long wave radiation emission from the surface [29, 30]. As defined by Reuter, Richardson [31], the two spectral channels of LDCM, centered near 10.9 and 12 microns, essentially double sample the single thermal band in the heritage TM/ETM+ systems. The bandwidths of LDCM in TIR region are narrower than of ETM+ and other broad band sensors that is used in SEBAL algorithm. Broadband emissivity is insensitive to surface temperature, for common surface temperatures [32], while narrow-bands emissivity are sensitive to LST and should be considered. This results in different responses from the surface, which in turn may alter the surface emissivity and temperature.

This study focuses on estimating the relationship between broadband and narrowband emissivity from the emissivities derived from the two LDCM thermal channels. On the other hand, this research investigates the effects of SRF and the effective wavelength on SEBAL-based LSE estimation method. In this paper, a modified SEBAL-based LSE estimate method,  $M_{\text{LSE-SEBAL}}$ , is adopted according to SRF of two narrow thermal bands of LDCM and is modified rather than initial LSE on broadband estimation.

This paper is organized as follows: In the introduction section, a brief description of the most common LSE estimation methods, as well as the objectives of this research is presented. In the sections, 2 and 3, after the presentation of data sets, pre-processing data are implemented. In section 4, the proposed methodology is explained in detail. In section 5, the results of the methods and experiments are analyzed and the final section, conclusions are given.

**II. STUDY AREA AND DATASETS**

The study area is an arid and semi-arid region, which is situated in the southern part of Iran. This area has various climate types with a diverse land cover including mixed pixels covered by different vegetation, soil, and rocky terrain types. It lies between latitudes 26° 25'–32° 44'N and longitudes 50° 32'–55° 54'E. The land use data, including seventeen classes provided by the ministry of Jihad and agriculture and one scene of LDCM data, Level 1T, captured on 14 June 2013 are shown in Fig. 1. Recently, the United States Geological Survey (USGS) on January 29, 2014, updated calibration parameters and Geometric alignment between the Operational Land Imager (OLI) and Thermal Infrared Sensor (TIRS) sensors of LDCM and changed the relative gains in the Calibration Parameter File (CPF) since launch. Therefore, USGS reprocessing scenes for on-demand product orders. In our research, LDCM data, Level 1T, captured on 23 June 2013 (and reprocessed by USGS based on calibration improvement parameters. ([http://landsat.usgs.gov/calibration\\_notices.php](http://landsat.usgs.gov/calibration_notices.php)).

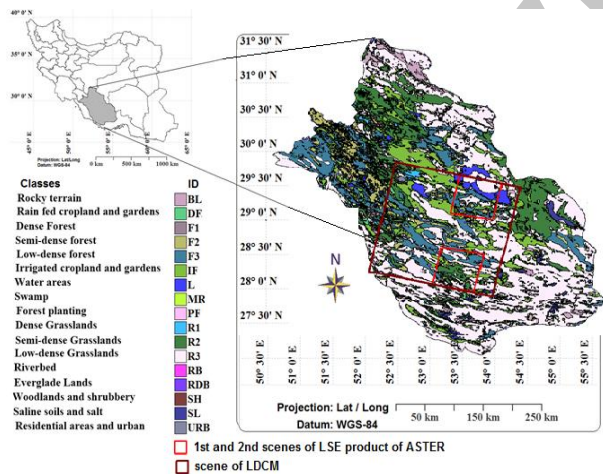


**Fig 1. The study area, land use data, Location of LDCM data and LSE product of ASTER that used in the study (provided by the ministry of Jihad and agriculture of Fars province).**

It is worth noting that LDCM datasets used in this study were ordered to be reprocessed by USGS based on calibration improvement parameters. Indeed, the United States Geological Survey (USGS) on January 29, 2014, updated calibration parameters and Geometric alignment between the OLI and TIRS sensors of LDCM and changed

the relative gains in the Calibration Parameter File (CPF) since launch. Therefore, USGS reprocessing scenes for on-demand product orders. In our research, LDCM data, Level 1T, captured on 23 June 2013 (and reprocessed by USGS based on calibration improvement parameters. ([http://landsat.usgs.gov/calibration\\_notices.php](http://landsat.usgs.gov/calibration_notices.php)). In this research, apart from the LDCM data, two scenes of the LSE standard product of Advanced Spaceborne Thermal Emission and Reflection Radiometer (ASTER) for LSE validation, was used. To evaluate all LSEs estimate methods (i.e. Modified and three compared LSE estimation methods), two LSEs standard products of ASTER as a reference was used for all methods. This product is generated from the ground surface emissivity (2B01T) data on 19 April 2013. The spatial resolution of this product is 90 m and was yielded by temperature emissivity separation (TES) algorithm. Based on numerical simulation, TES can recover LST within about ±1.5 K, and LSE within about ±0.015[20]. The [33] points out that the LSEs estimate by the ASTER TES algorithm is usually in qualitative agreement with field or laboratory measurements. Therefore, the estimated LSEs achieved by all methods are compared with this product for the whole image in terms of root mean square error (RMSE) measure in corresponding thermal bands.

**III. CHANNEL EMISSIVITY AND DATA PRE-PROCESSING**

*A. Channel emissivity*

Similar to channel radiance, channel emissivity can be defined by convolving spectral emissivity with the normalized channel response function. Ideally, the convolution should also include the temperature dependency via the Planck's function,  $B_{\lambda}(T_s)$ , for black body emission. By definition, the channel emissivity ( $\epsilon_i$ ) for a specified sensor is given by [1, 34, 35]:

$$\epsilon_i = \frac{\int_{\lambda_1}^{\lambda_2} \epsilon(\lambda) R_i(\lambda) B_{\lambda}(T_s) d\lambda}{\int_{\lambda_1}^{\lambda_2} R_i(\lambda) B_{\lambda}(T_s) d\lambda} \tag{1}$$

Where  $\lambda$  denotes wavelength,  $B_{\lambda}(T_s)$  is the Planck's function for black body emission,  $R_i(\lambda)$  is the normalized spectral response function (SRF) of the sensor in channel  $i$  and  $\epsilon(\lambda)$  is the spectral emissivity for various surfaces can be obtained by field or laboratory measurements,  $\lambda_1$  and  $\lambda_2$  are referred to the lower and upper wavelength for the corresponded spectral domain. Although in Equation (1),  $\epsilon_i$  depends on LST, however, in a terrestrial temperature range, LSE is almost independent of LST [36], and so the variation of  $\epsilon_i$  with LST is negligible ( $\Delta\epsilon=10^{-4}$ ). Therefore, the channel emissivity can be expressed as Equation. (2).

$$\varepsilon_i = \frac{\int_{\lambda_1}^{\lambda_2} \varepsilon(\lambda) R_i(\lambda) d\lambda}{\int_{\lambda_1}^{\lambda_2} R_i(\lambda) d\lambda} \quad (2)$$

The main problem in determining emissivity from Equation (2) is the observation of emissivity of natural surfaces at satellite spectral and spatial resolutions [1]. LSEs and specially LST can vary due to shadowing effects and topographic effects [37]. Therefore, it is necessary that atmospheric correction, shadow removal and topographic correction apply to the data. As can be seen in Equation (2) and (3), LSE is depending on the effective wavelength of the thermal band and SRF of sensors. Figure 2, shows a comparison of the TIRS spectral bandwidths of LDCM with the previous Landsat thermal channel (ETM<sup>+</sup>).

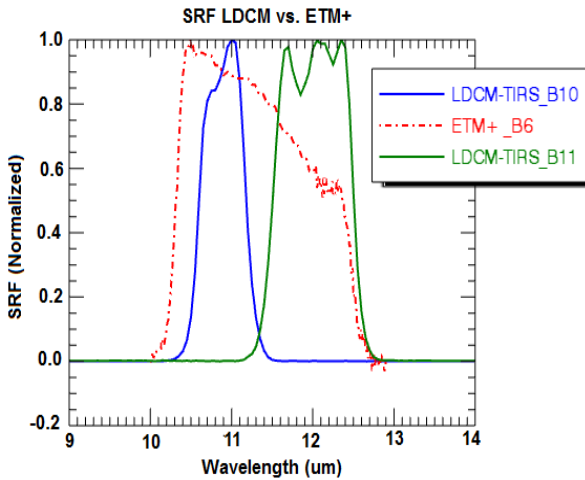


Fig. 2. Comparison of the relative spectral response of the LDCM TIRS thermal channels with the previous Landsat instrument (ETM<sup>+</sup>) (SRF data from USGS).

According to researchers [38, 39], the effective wavelength is defined by the following equation:

$$\lambda_{eff} = \frac{\int_{\lambda_1}^{\lambda_2} \lambda_i R_i(\lambda) d\lambda}{\int_{\lambda_1}^{\lambda_2} R_i(\lambda) d\lambda} \quad (3)$$

Where, R is the normalized SRF of the thermal band, which is given with discrete pattern and in finite range.

Consequently, estimating the effective wavelength is an issue that is how to tackle the discrete integration properly, which is also called ‘numerical integration’. More explanation and the calculation methods of effective wavelength is provided by [38]. The effective wavelengths of TIRS/LDCM are 10.9036 μm and 12.0030 μm for bands 10 and 11, respectively[40]. In addition, it is 11.256 μm for thermal band 6 of ETM<sup>+</sup>[41].

In this study, the ASTER spectral library (v2.0), ranging from 0.4 to 14 μm is used for the spectral emissivity of classes in thermal (10.60 - 11.19 μm) and (11.50 - 12.51 μm) spectral ranges from Kirchhoff’s law (Emissivity=1-Reflectance). This library was measured in directional hemispherical reflectance under most conditions that the infrared portion of these data can be used to calculate emissivity using Kirchhoff’s Law, which has been verified by both laboratory and field measurements [42, 43].

This library includes data from three other spectral libraries: the Johns Hopkins University (JHU), the Jet Propulsion Laboratory (JPL), and the United States Geological Survey (USGS) Spectral Library [44, 45]. Then, the spectral emissivity of each spectrum is computed by Kirchhoff’s law in the thermal range of TIRS on LDCM. On the other hand, we simulated TIRS/LDCM channel emissivities of band 10 and 11 using Equation (2) from the ASTER spectral library for all the samples of rocks, soils, vegetation, water and so on. The obtained emissivities of seventeen classes along with their standard deviations in TIRS bands of LDCM are given in Table I. At first, main classes such as forest, grasslands, rocky, water, soil, vegetation, dry vegetation and mineral are obtained from the ASTER spectral library by Equation. (2). Moreover, the emissivity values of two classes ( woodlands-shrubbery and saline soils-salt) are obtained from [46]. Then, the emissivity values for combined classes experimentally set as follows (Table I). It is noteworthy that emissivity values of combined classes only was used for classification based emissivity method (CBEM) in this study.

The choice of a typical emissivity value for some surface objects such as soil is a more critical question, because the variability of emissivity values for soils is more than vegetation and other ones [47]. In order to estimate the emissivity of a given class, initially the  $\varepsilon_\lambda$  of a set of similar classes (e.g. 113 spectral emissivities was chosen for soils class) are selected from the ASTER spectral library. Therefore, the mean value of spectral emissivities is considered for the emissivity of each class. After calculating the emissivities for the classes, radiometric correction was conducted, the emissivities of the LDCM data through three compared, and one modified proposed LSE estimation methods were determined.

**Table I. Emissivities of classes in band 10 and 11 of LDCM data**

Class	source of emissivity value	<sup>a</sup> $\epsilon_{10}$	<sup>b</sup> $\sigma_{10}$	$\epsilon_{11}$	$\sigma_{11}$
Dense Forest	ASTER spectral library	0.9817	0.0080	0.9842	0.0095
Semi-dense forest	(Emis_soil + Emis_forest)/2	0.9787	0.0071	0.9821	0.0079
Low-dense forest	(2*Emis_soil + Emis_forest)/3	0.9757	0.0061	0.9800	0.0063
Irrigated cropland and gardens	(Emis_water + Emis_soil + Emis_forest)/3	0.9863	0.0080	0.9852	0.0095
Dense Grasslands	ASTER spectral library	0.9833	0.0080	0.9886	0.0095
Semi-dense Grasslands	(Emis_soil + Emis_Grasslands)/2	0.9799	0.0040	0.9854	0.0033
Low-dense Grasslands	(2*Emis_soil + Emis_Grasslands)/3	0.9765	0.0066	0.9821	0.0071
Rocky terrain	ASTER spectral library	0.9613	0.0129	0.9544	0.0094
Rain fed cropland and gardens	(Emis_Veg + Emis_soil + Emis_forest)/3	0.9757	0.0041	0.9800	0.0051
Everglade Lands	(Emis_water + Emis_forest)/2	0.9871	0.0041	0.9852	0.0051
Woodlands and shrubbery	From Reference [46]	0.9700	0.0051	0.9770	0.0047
Residential areas and urban	ASTER spectral library	0.9479	0.0151	0.9541	0.0149
Forest planting	ASTER spectral library	0.9787	0.0059	0.9822	0.0047
Swamp	(Emis_Veg + Emis_dry.veg + Emis_water)/3	0.9752	0.0048	0.9772	0.0075
Saline soils and salt	From Reference [46]	0.9650	0.0041	0.9710	0.0031
Water areas	ASTER spectral library	0.9909	0.0001	0.9861	0.0007
Riverbed	(Emis_water + Emis_mineral)/2	0.9657	0.0027	0.9759	0.0021

a, channel emissivity; b, standard deviation of the channel emissivity

### B. Data pre-processing

Obviously, in order to use satellite-imaging data for quantitative remote sensing of land surfaces, the atmospheric and topographic effects must be removed. An effective removal of atmospheric and topographic effects on remote-sensing imagery is an essential pre-processing step for deriving a good estimate of physical parameters of the earth's surface, i.e. surface spectral reflectance, emissivity and temperature. The various techniques that remove these effects have been proposed and consist of

specific combinations of an atmospheric and a topographic correction method. Atmospheric and Topographic Correction (ATCOR) is a method used to eliminate atmospheric and illumination effects on satellite imagery. In this study, ATCOR23, independent interactive data language (IDL) programming based on MODTRAN-4, is used for atmospheric correction of rugged terrain by integrating ASTER digital elevation model (DEM).

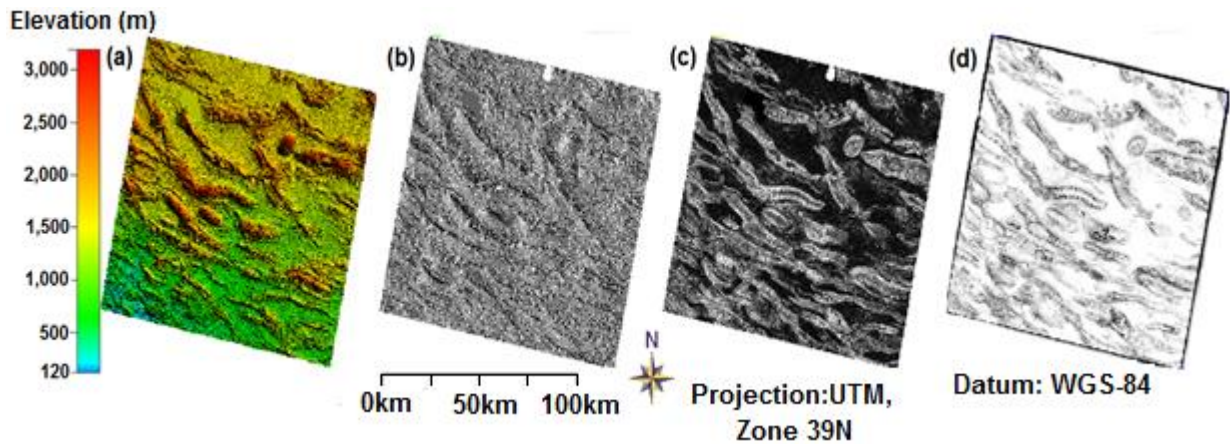


Figure 3. DEM and its derivatives in a part of the image: (a) DEM (b) slope, (c) slope, (c) sky view.

Then, using the ATCOR23, topography and atmospheric correction were performed over the LDCM image. ATCOR23 has two separate options: ATCOR 2 and ATCOR3. ATCOR 2 is used for atmospheric correction in the flat area and ATCOR3 includes all of the capabilities of ATCOR2 and can be integrated with a DEM for atmospheric correction of images depicting rugged terrain[18]. It employs a large high-resolution atmospheric database, compiled using the “MODerate spectral resolution atmospheric TRANsmittance algorithm and computer model” (MODTRAN) code employing DISORT, 8stream option (DIScrete Ordinate Radiance Transfer) for computing multiple scattering components of the total path radiance [18, 48]. In this study, sensor and image information (such as solar and the sensor zenith angle at the

time of data acquisition, azimuth angle of solar and sensor, the date and time of image acquisition, pixel size, calibration file include gain /offset of bands and etc.) from metafile of images were introduced to ATCOR. In addition, it uses the algorithm dark dense vegetation (DDV) to estimate the atmospheric optical thickness or visibility [18, 49]. Moreover, atmospheric and aerosol model based on the longitude of the study area and date and time of image acquisition was determined and were introduced to ATCOR. Figure 4 shows these corrections on the part of the image. It is noteworthy that sky-view factor can be used as a general relief visualization technique to show relief characteristics. In particular, this visualization is a very useful tool in the recognition of small scale features from high-resolution DEMs [50].

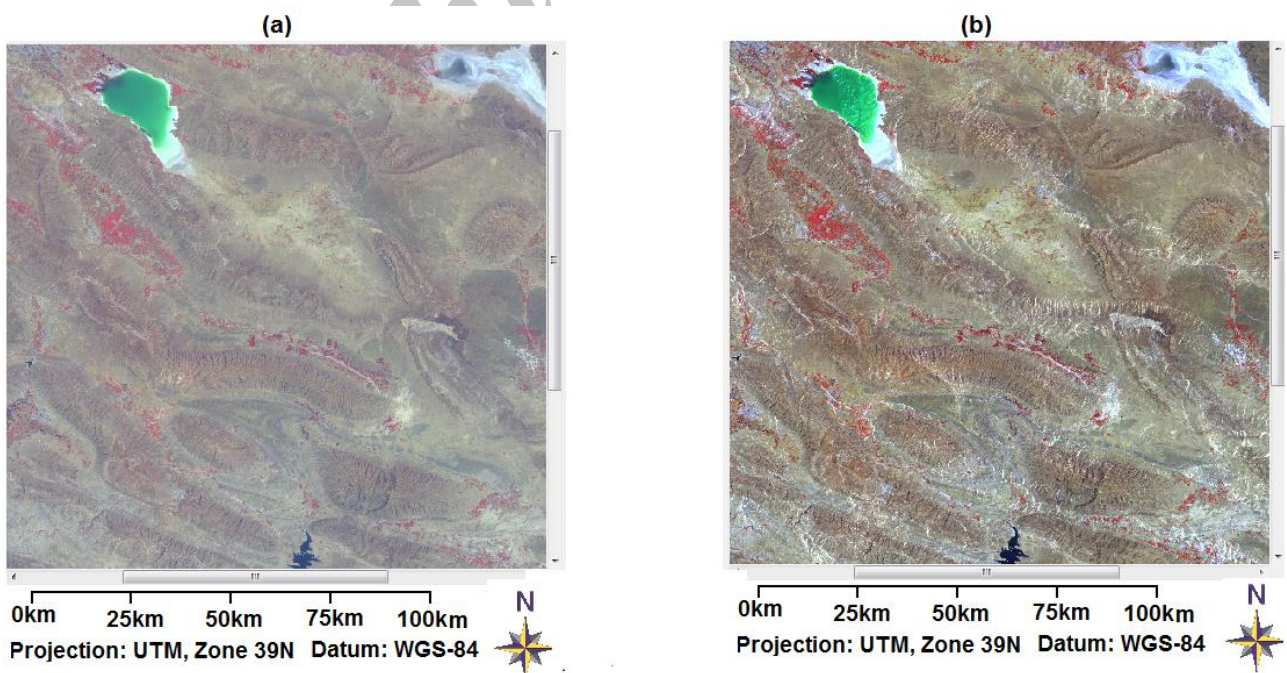


Fig. 4. Topographic and atmospheric correction are shown in the partly of the images: (a) original image, (b) corrected image.

**IV. THE MODIFICATION OF SEBAL METHODOLOGY**

The SEBAL was provided by [11] which uses spectral radiances, together with weather and climate data, to solve the energy balance Equation at the earth's surface. Several common vegetation indices are used in the SEBAL method. Normalized Difference Vegetation Index (NDVI), Modified Soil Adjusted Vegetation Index (MSAVI), Weighted Difference Vegetation Index (WDVI), and Leaf Area Index (LAI) indices are computed using the reflectance values. Indeed, NBEM and SEBAL are vegetation-based LSE estimation methods. The NBEM use only one vegetation index (NDVI), while SEBAL utilizes several vegetation indices (SAVI, NDVI, and LAI). The various studies [51-53] stated that the aim of using the several vegetation indices is minimized soil background and brightness effects on LAI. In this study area, pixels usually contain a mix of vegetation and soil context. SEBAL and twenty-five their computational sub-models calculate different surface variables [28]. Many studies have been used to compute LSE from the SEBAL method [30, 54]. One of the sub-model of this algorithm is for LSE estimation in the wider broadband that shown in Equation (4).

$$\begin{aligned}
 \epsilon_{NB}^{B6} &= 0.97 + 0.0033 LAI \quad ; \quad (NDVI > 0 \ \& \ LAI < 3) \\
 \epsilon_{NB}^{B6} &= 0.98 \quad ; \quad (NDVI > 0 \ \& \ LAI \geq 3) \\
 \epsilon_{NB}^{B6} &= 0.99 \quad ; \quad (NDVI < 0)
 \end{aligned}
 \tag{4}$$

SEBAL algorithm not only has been used for different data from satellite remote sensing with wide broadband (3-14 μm), but also it is used in calculating the LSE and LST in the relatively wide broadband (8-14 μm) spectral range. The Landsat 8 satellite (LDCM) with two thermal infrared bands provided another opportunity for the estimation of LSE and LST. In the LDCM, the (8-14 μm) spectral range divided into the narrow ranges of thermal bands. Therefore, the use of the primary SEBAL algorithm is not true and causes errors in LSE and LST estimation. Therefore, this algorithm should be modified and corrected rather than to narrow thermal bands of LDCM. It is worthy to note that the LAI in Equation (4), is computed through MSAVI using the empirical equation proposed by [55].

In this research, the implementation of the modified LSE estimation methodology, M<sub>LSE</sub>-SEBAL, consists of four steps as in the following flowchart in order to improve the LSE estimates for the LST retrieval (Fig. 5).

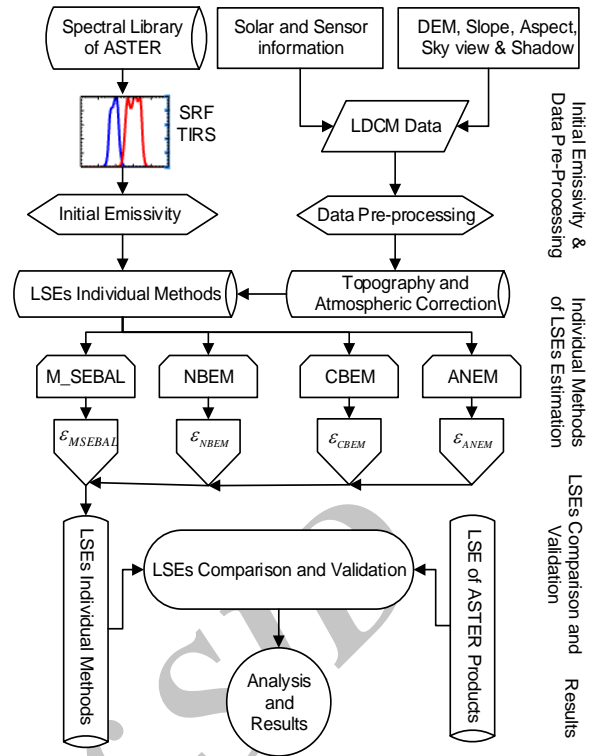


Fig. 5. The flowchart of proposed methodology in this study

In the first step, the initial values of emissivities have been calculated for all land use classes using the ASTER spectral library as aforementioned and data pre-processing including atmospheric and topographic correction were conducted. In the second step, modification SEBAL-based and three other compared LSE estimation methods were applied based on TIR bands of LDCM. These methods include (i) NBEM, (ii) M<sub>LSE</sub>SEBAL, (iii) CBEM, and (iv) ANEM. In the third step, for LSE validation, the LSEs obtained by M<sub>LSE</sub>SEBAL proposed and three individual methods were compared with earth surface emissivity (2B04) standard product of Advanced Spaceborne Thermal Emission and Reflection Radiometer (ASTER). In the final step, the results of the methods and experiments are analyzed and conclusions are given.

Two emissivities are used in initial SEBAL algorithm which the first emissivity represents the surface behaviour for thermal emission in long wave infrared (LWIR)(8-14μm) that expressed as ε<sub>NB</sub>, and the second emissivity represents the surface behaviour for thermal emission in the broad thermal spectrum (3-14 μm) is used to estimate the net longwave radiation. In this research focused on this emissivity. The first emissivity is used in the calculation of the LST. To this end, ε<sub>NB</sub> for the according to their SRF of TIR bands of LDCM has been modified by using the ASTER spectral library. The spectra of rocks, soils, vegetation, water, so on, which are essential components of the terrestrial ecosystem, are collected in this study. In total

257 spectral samples from the ASTER Spectral library are used to develop our modification method. The ASTER library contains directional hemispherical spectral reflectance; therefore, we converted to spectral emissivity using Kirchhoff's law. In the current study, according to the SRF of two very narrow TIR bands of LDCM, (10.60 - 11.19 μm) and (11.50 - 12.51 μm) spectral ranges, the emissivity, ε<sub>NB</sub>, were yield as Equations (5).

$$\begin{cases} \epsilon_{NB_{10}}^{TIRS} = 0.969781 + 0.004100 LAI \\ \epsilon_{NB_{11}}^{TIRS} = 0.976116 + 0.003106 LAI \end{cases} ; (NDVI > 0 \ \& \ LAI < 3)$$

$$\begin{cases} \epsilon_{NB_{10}}^{TIRS} = 0.98173200 \\ \epsilon_{NB_{11}}^{TIRS} = 0.98425133 \end{cases} ; (NDVI > 0 \ \& \ LAI \geq 3) \quad (5)$$

$$\begin{cases} \epsilon_{NB_{10}}^{TIRS} = 0.99085700 \\ \epsilon_{NB_{11}}^{TIRS} = 0.98985167 \end{cases} ; (NDVI < 0)$$

with assuming the spectral response is rectangle, the broadband emissivity can also be written by [34]

$$\epsilon_i = \frac{\int_{\lambda_1}^{\lambda_2} \epsilon(\lambda) R_i(\lambda) d\lambda}{\int_{\lambda_1}^{\lambda_2} R_i(\lambda) d\lambda} = \sum_{i=1}^{i=n} g_i \epsilon'_i \quad (6)$$

With

$$\epsilon'_i = \frac{\int_{\lambda^{(i)}}^{\lambda^{(i+1)}} \epsilon_{\lambda} B_{\lambda}(T) d\lambda}{\int_{\lambda^{(i)}}^{\lambda^{(i+1)}} B_{\lambda}(T) d\lambda} \quad (7)$$

$$g_i = \frac{\int_{\lambda^{(i)}}^{\lambda^{(i+1)}} B_{\lambda}(T) d\lambda}{\int_{\lambda_1}^{\lambda_2} B_{\lambda}(T) d\lambda} \quad (8)$$

Equation 6 shows that the broadband emissivity is linearly related to the narrowband channel emissivities with coefficients g<sub>i</sub> nearly independent on the surface temperature [34]. Therefore, other researchers also linear formula implanted between broadband and narrow bands emissivities [26, 56]. According to this, in this study, we have assumed a linear relationship between the broadband and narrow bands (i.e. initial SEBAL-based LSE estimation method and modification M<sub>LSE</sub>SEBAL methodology) emissivities.

$$\epsilon^{BroadBand} = \sum_{ch=10}^{11} a_{ch} \times \epsilon_{ch}^{NarrowBand} + c \quad (9)$$

We calibrated the linear regression using the ASTER spectral Library. The calibrated coefficients were a<sub>10</sub>-a<sub>11</sub> as 0.8049, and 1.2733E-11, respectively, and c as 0.1894. The RMSE in calibration and validation of Equation. (9) were 1.5692E-13.

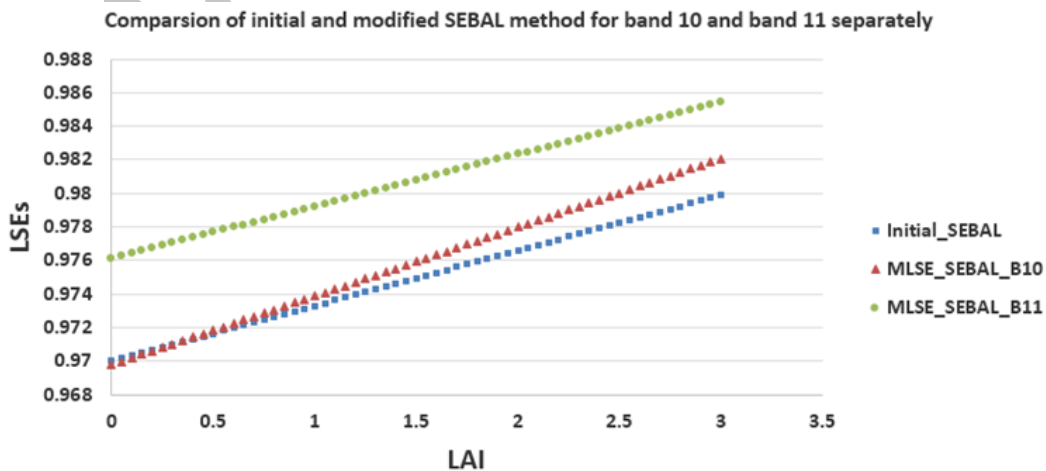


Fig. 6. Comparison of initial and modified SEBAL method for band 10 and 11 of LDCM.

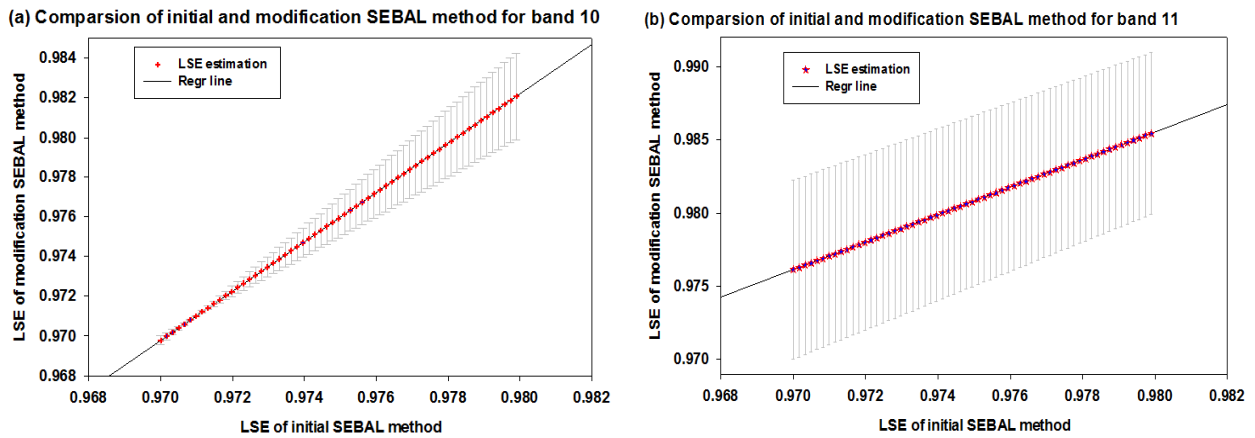


Fig. 7. Comparison of initial and modification SEBAL method in the vegetated and non-vegetated areas, (a) for band 10 of LDCM, (b) for band 11 of LDCM

By comparing achieved LSEs of initial SEBAL-based and modified methods in the Figures 6 and 7a, b, it can be seen the effects of SRF, effective wavelengths, physical and vegetation of earth’ surface parameters in the LSE estimation by SEBAL algorithm. Effective wavelength is relatively close together in the initial and band 10 of modified SEBAL method. Therefore, the LSE estimation in the non-vegetated area is almost identical and there is no significant difference, while it is different in the vegetated area. The difference between vegetated areas and non-vegetated areas can be easily seen from LAI index. These changes are the result of the impact of environmental parameters such as moisture, texture, the canopy of vegetation and SRF, which can be affected on the LSE estimation. Moreover, by comparison, achieved LSEs of primary SEBAL-based and band 11 of  $M_{LSE}$ SEBAL methods in the Figures 6 and 7a, b, it can be seen that there is a relatively large difference in the effective wavelength and SRF between them. In this case, areas with vegetation and no vegetation have the same performance and the greatest difference in LSE estimation. On average, there are 0.22% and 0.61% improvement between initial and modified SEBAL methodology for band 10 and band 11, respectively.

As previously mentioned, a few studies have shown that an error of 1 % in the LSE can lead to an error in the LST ranging from 1 K to 2 K in LST using single channel (SC) algorithm around 10 microns [2]. Thus, a small improvement in LSE can influence LST remarkably. Although broadband emissivity varies greatly with location, especially in non-vegetated area, while narrowband emissivity has tangible variation in the areas with dense vegetation. These changes can be the effects of SRF and effective wavelengths in the impact of environmental parameters for LSE estimation.

### A. LSE Comparison and Validation

In this part, for comparison and validation of the proposed  $M_{LSE}$ SEBAL method, other three common LSE estimation methods, including (i) NBEM, (ii) CBEM, (iii) ANEM were implemented as follows.

#### 1) NDVI Based Emissivity Method (NBEM)

Different approaches have been used to predict LSE from NDVI values [9, 10, 57-61]. Fully vegetated areas are approximate blackbodies and the emissivity spectrum is nearly constant and near unity. Therefore, estimating the emissivity spectrum of these types of surface is less important than for surfaces of soils or rock. In fact, the NDVI approach assumes a constant value of emissivity for these areas. In the over particular areas,  $NDVI_{veg}$  and  $NDVI_{soil}$  values can be extracted from the NDVI histogram that was proposed by Sobrino, Jiménez-Muñoz [9]. For those pixels composed of soil and vegetation (mixed pixels,  $NDVI_{soil} < NDVI < NDVI_{veg}$ ), the method uses the following simplified Equation (10).

$$\epsilon_{\lambda_i (mix)} = \epsilon_{\lambda_i (veg)} \cdot P_v + \epsilon_{\lambda_i (soil)} (1 - P_v) + C_{\lambda_i} ; i=1,2 \quad (10)$$

Where  $\epsilon_{veg}$  and  $\epsilon_{soil}$  are the soil and vegetation emissivities, respectively.  $i$  refers to two thermal bands of TIRS sensor of LDCM,  $P_v$  is the proportion of vegetation (also referred to as fractional vegetation cover, FVC), and  $C$  is a term which takes into account the cavity effect due to surface roughness. Using the geometrical model proposed by the [9], the cavity term for a mixed area and near-nadir view is given by:

$$C_{\lambda_i} = (1 - \epsilon_{\lambda_i (soil)}) \cdot \epsilon_{\lambda_i (veg)} F' \cdot (1 - P_v) ; i=1,2 \quad (11)$$

Where  $F'$  is a geometrical factor ranging from zero to one, depending on the geometrical distribution of the surface [62]. Since  $F'$  cannot be estimated from VNIR/TIR data, a

mean value is chosen. Moreover,  $P_v$  values are obtained from the NDVI according to Equation (12) [63].

$$P_v = \left( \frac{NDVI - NDVI_{soil}}{NDVI_{veg} - NDVI_{soil}} \right)^2 \quad (12)$$

In this study, NBEM proposed by [9] was used.

$$\varepsilon_{\lambda_i} = \begin{cases} \varepsilon_{\lambda_i(veg)} \cdot P_v + \varepsilon_{\lambda_i(soil)} (1 - P_v) + C_{\lambda_i}, & NDVI_{soil} \leq NDVI \leq NDVI_{veg} \\ \varepsilon_{\lambda_i(soil)}, & NDVI < NDVI_{soil} \\ \varepsilon_{\lambda_i(veg)}, & NDVI > NDVI_{veg} \\ \varepsilon_{\lambda_i(water)}, & \text{masked water area} \end{cases} \quad i=1,2 \quad (13)$$

The water body areas in each scene masked and their emissivities were assigned independently. In other areas,  $NDVI_{veg}$  and  $NDVI_{soil}$  were determined by the NDVI histogram and the  $NDVI_{soil}$  and  $NDVI_{veg}$  values were set to 0.20 and 0.50, respectively.

### 2) Classification Based Emissivity Method (CBEM)

Generally, CBEM uses conventional land cover data. This method assumes that similarly, classified land covers types exhibit very similar LSEs [1, 12, 13, 64, 65]. DEM-based topographic corrections on satellite imagery from rugged terrain, as effective processing techniques to improve the accuracy of Land Use/Land Cover (LULC) classification as well as land surface parameter retrievals with remotely sensed data [66]. As is widely known, the pixel-based image classification approach classifies remote sensing images according to the spectral information in the image 'pixel by pixel'. In this study, atmospheric and topographic corrected image was classified using a Maximum Likelihood Classification (MLC) algorithm. The authors are aware of some limitations to the 'per pixel approach' [67], but in this case the MLC produced very satisfactory results. Then, the obtained initial emissivities from Table I assign to each pixel according to its class label. The overall accuracy (OA) of classified image is about 91.21 %.

### 3) Adjusted Normalization Emissivity Method (ANEM)

This Normalization Emissivity Method (NEM) assumes a constant emissivity in all channels for a given pixel, provided that the atmospheric effects are corrected [17]. In the adjusted NEM (ANEM) the assigned emissivity is surface cover dependent [18]. The ANEM is based on the combination of the vegetation cover method (VCM)

and the Normalized Emissivity Method (NEM). This method uses of the VI and NIR data to estimate the vegetation cover and assigned the maximum emissivity based on VCM. ANEM, instead of using a fixed value of emissivity, sets the initial value of emissivity regarding the spatial variation of emissivity with VCM. Estimating channel emissivities in a pixel-by-pixel way can be done by VCM, using coefficients fit in each band. In this study, ANEM is implemented based on the mathematical structure proposed by [16] and [68]. For each channel, the maximum emissivities from the ASTER spectral library are assigned to class emissivities according to SRF of TIRS /LDCM.

## B. LSE Validation

### 1) Image-Based Cross-Validation (IBCV)

There are two procedures to validate the LSE values retrieved from space [59, 69]. The first, known as the direct method, directly compares the ground-based measurements with satellite-derived products. The second, known as the indirect method, indirectly validates the non-validated product with the various satellite-derived products, model simulations, or other information and applications. The studies by [33] points out that the LSEs estimate by the ASTER TES algorithm is usually in qualitative agreement with field or laboratory measurements. In the current study, indirect method of LSE is used and the achieved LSEs of bands 10 and 11 in the LDCM data were compared with the corresponding LSE standard product of ASTER (i.e. bands 13 and 14) in the whole image that is known to Image-Based Cross-Validation (IBCV). To evaluate and validation of all LSE estimation methods (i.e. three common compared and modified proposed methods), two LSE standard products of ASTER were used as a reference for all methods. This product was generated from the ground surface emissivity (2B01T) data on 19 April 2013. Moreover, the spatial resolution of this product is 90m and was obtained by the TES process.

Therefore, the achieved LSEs by the three compared along with  $M_{LSE}$  SEBAL LSE estimation methods are compared to each other with corresponding thermal bands of the ASTER product for the whole image in terms of RMSE. The obtained results of IBCV are shown in Fig. 8a, b, and Fig. 9a, b, in the first and second scenes of ASTER, respectively.

The same calculation is performed on the second scene of ASTER product and the results for RMSE measure are given in Fig. 9a, and b.

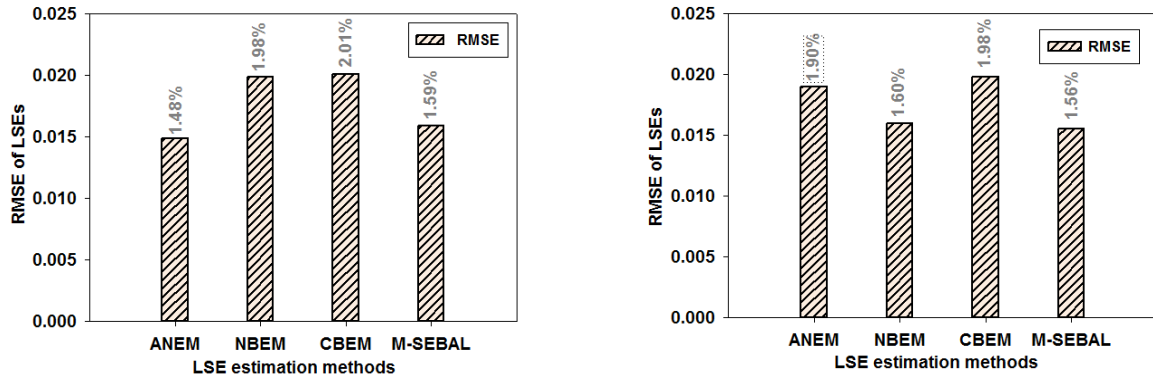


Fig. 8. IBCV of LSEs of bands 10 and 11 in the LDCM data for compared and proposed methods in first examined scene. (a) RMSE of LSEs for band 10, (b) RMSE of LSEs for band 11.

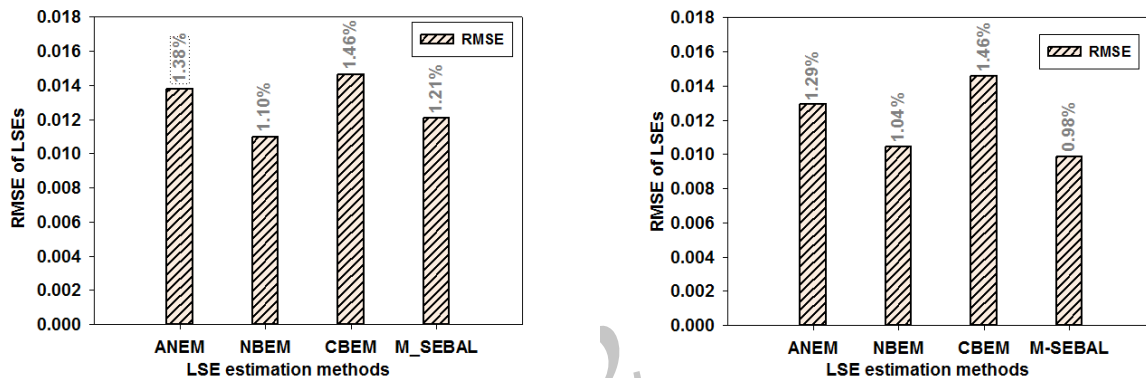


Fig. 9. IBCV comparison of LSEs of bands 10 and 11 in the LDCM data for compared and proposed methods in the second examined scene. (a) RMSE of LSEs for band 10, (b) RMSE of LSEs for band 11.

As illustrated in Fig. 8a, b, and Fig. 9a, b, the results of the three common compared methods are worse than the result obtained by the  $M_{LSE}SEBAL$  proposed method. Moreover, in  $M_{LSE}SEBAL$  method almost displayed appropriate performance in term of RMSE measure. The results show that the RMSE of LSE obtained by  $M_{LSE}SEBAL$  method is 1.59% and 1.21% in thermal band 10 of the first and second examined scenes, respectively. Moreover, for the thermal band 11, the error values of  $M_{LSE}SEBAL$  method are 1.56% and 0.98% in the two examined scenes, respectively. Generally, the experimental results demonstrated that the  $M_{LSE}SEBAL$  perform significantly better than the compared methods for LSE estimation. Moreover, We conducted the LSE validation, on the whole image in initial and modified SEBAL-based LSE estimation in comparison with two scenes the LSE product of ASTER in term of RMSE measures, and the results were given in Fig. 10a, b, c, d and Fig. 11a, b, c, d, in the first and second scenes of ASTER, respectively.

As illustrated in Fig. 10a, b, c, d and Fig. 11a, b, c, d the results of the modified SEBAL-based LSE estimation method is better than the result obtained by the initial SEBAL method in term of RMSE measure.

## 2) Class-Based Cross-Validation (CBCV)

To investigate the effects of surface parameters on LSE estimation by three compared and  $M_{LSE}SEBAL$  methods, an assessment was conducted in each class. In this regard, the CBCV was performed on the available classes based on land use data in the corresponding thermal bands of the LDCM and ASTER data. The results are shown in Fig. 12a, b, and Fig. 13a, b in term of RMSE.

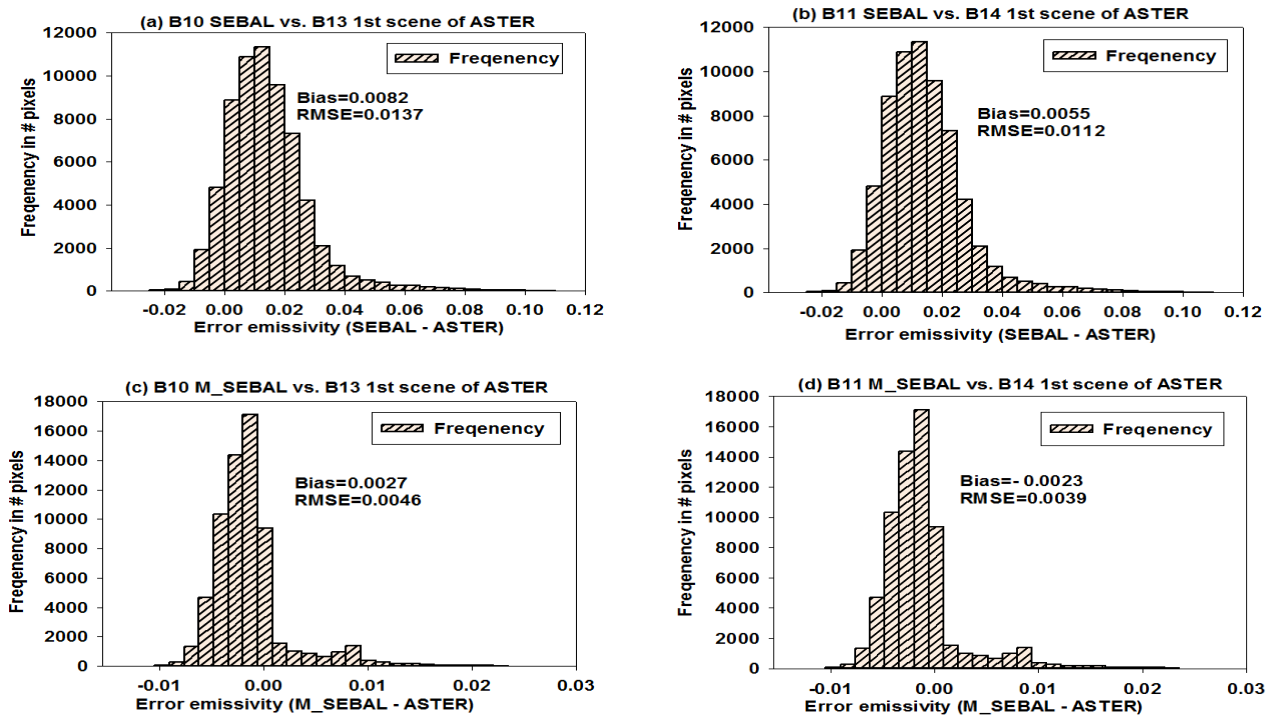


Fig. 10. Cross-comparison of the initial and modified SEBAL-based LSE estimation methods in the first examined scene. (a) and (b) Error emissivity of initial SEBAL method for band 10, and band 11, respectively, (c) and (d) Error emissivity of  $M_{LSE}SEBAL$  for band 10 and band 11, respectively.

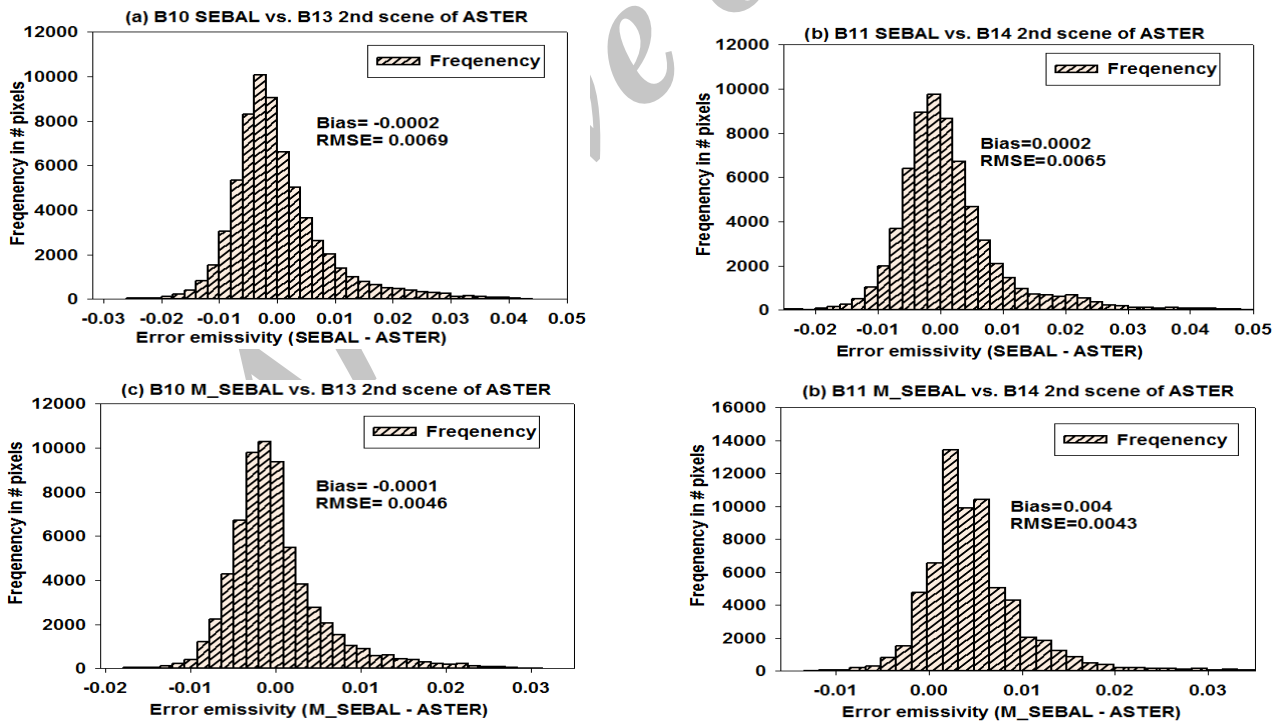


Fig. 11. Cross-comparison of the initial and modified SEBAL-based LSE estimation methods in the second examined scene of ASTER. (a) and (b) Error emissivity of initial SEBAL method for band 10, and band 11, respectively, (c) and (d) Error emissivity of  $M_{LSE}SEBAL$  for band 10 and band 11, respectively.

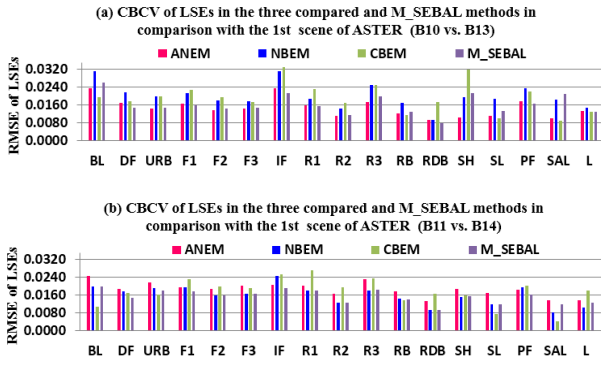


Fig. 12. CBCV of the three compared and modified SEBAL-based LSE estimation methods in comparison of the first examined scene of ASTER in term of RMSE. (a) Error emissivity for band 10, (b) Error emissivity for band 11.

Fig. 12a and b show the comparison results of compared and modified methods in each class in terms of RMSE for bands 10 and 11, respectively. The same calculation was performed on the second ASTER scene and the results are given in terms of RMSE in Fig. 13a and b for bands 10 and 11, respectively.

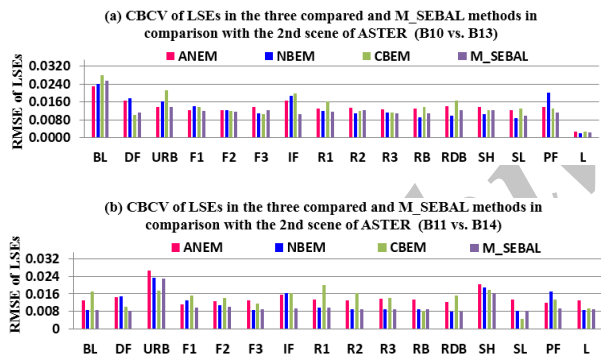


Fig. 13. CBCV of the three compared and modified SEBAL-based LSE estimation methods in comparison of the second examined scene of ASTER. (a) Error emissivity for band 10 in term of RMSE, (b) Error emissivity for band 11 in term of RMSE.

There are a consistent result among the compared and modified SEBAL-based LSE estimation methods in non-vegetation classes like L class or classes which, consist of lower vegetation density and high fraction soil such as F3, R3 and URB classes. In contrast, the obtained results of CBCV (Fig. 12a, b and Fig. 13a, b) showed that in classes that consist density vegetation the  $M_{LSE}SEBAL$  and NBEM demonstrated almost the same results and better performance rather than ANEM and CBEM methods. These changes are the result of the impact of environmental parameters such as moisture, texture, canopy of vegetation and SRF, which can be effect on the LSE estimation.

### 3) The Sensitivity Analysis of LSE Improvement on LST

Having LSEs, the LST can be retrieved by different methods. There are many LST retrieval methods for Landsat data in the literature [70-74]. Landsat 4 and 5, and following by Landsat 7, there was only one thermal infrared channel available [75, 76]. Therefore, a single-channel (SC) algorithm was developed to derive LST from this band. Influential researchers were conducted mainly by [39, 47, 77] and [78]. In [47] three famous SC algorithms, (i) the radiative transfer equation, (ii) Qin et al.'s algorithm, and (iii) Jimenez-Munoz and Sobrino's ( $SC^{JM\&S}$ ) algorithm, to retrieve the LST from the single thermal band are compared. The  $SC^{JM\&S}$  algorithm shows a good performance for water vapor content values between 0.5 and 2  $g \cdot cm^{-2}$ , with RMSE values below 1 K [77]. In contrast to previous Landsat satellites, the TIRS of LDCM data contains two thermal channels, which split-window (SW) and SC algorithms are capable of utilizing for LST retrieval [79]. Considering the strip problem, ghost signal caused by stray light and a time-varying absolute calibration error for TIRS, the validation exercise is still a tough problem [80]. Therefore, based on the USGS recommendation on the LDCM data, the SC algorithm of [39] is used. To this end, to evaluate the impact of the LSE improvement on LST, the  $SC^{JM\&S}$  algorithm of [39] is used. SC algorithm is utilized for sensitivity analysis using only band 10. Therefore, the  $\sigma_{alg}$  is below 1 K since the VW content of the study area is 1.2 for the examined dataset (Table II). The  $SC^{JM\&S}$  algorithm retrieves LST ( $T_s$ ) using the general Equation (14).

$$T_s = \left( \left\{ \frac{k_2 L_{sen}}{T_{sen}^2} \left[ \frac{\lambda_e^4}{k_1} + \lambda_e^{-1} \right] \right\}^{-1} \right) \left[ \frac{1}{\varepsilon} (\psi_1 L_{sen} + \psi_2) + \psi_3 \right] + (T_{sen} - \gamma L_{sen}) \quad (14)$$

where  $L_{sen}$  is the at-sensor radiance in  $w m^2 sr^{-1} \mu m^{-1}$ ,  $T_{sen}$  is the at-sensor brightness temperature in K,  $\lambda_e$  is the effective wavelength in  $\mu m$ ,  $k_1$  and  $k_2$  are constant of thermal bands in  $W m^2 sr^{-1} \mu m^{-1}$  and K, respectively.  $\varepsilon$  is the surface emissivity and unitless,  $\psi_1$ ,  $\psi_2$ , and  $\psi_3$  are referred to as atmospheric functions (AFs) which computed by Equation (15) [79].

$$\psi_1 = \frac{1}{\tau}, \quad \psi_2 = -L \downarrow - \frac{L \uparrow}{\tau}, \quad \psi_3 = L \downarrow \quad (15)$$

Where  $L \uparrow$  is the upwelling radiation and  $L \downarrow$  is the downwelling radiation in  $w m^2 sr^{-1} \mu m^{-1}$  and  $\tau$  is unitless and atmospheric transmittance.

**Table II. Atmospheric parameters for LDCM<sup>a</sup>**

Scene	$\tau$	$L^\uparrow$	$L^\downarrow$	WV
162-40	0.85	1.19	1.98	1.20

a.  $\tau$  , atmospheric transmissivity;  $L^\uparrow$  , upwelling radiation;  $L^\downarrow$  , downwelling radiation; WV , water vapor

For each image,  $\tau$ ,  $L^\uparrow$  and  $L^\downarrow$  were obtained using online radiative transfer codes (<http://www.atmcorr.gsfc.nasa.gov/>) from Atmospheric Correction Parameter Calculator (ACPC) developed by NASA for Landsat satellites [81, 82] (Table II). Validation of ACPC parameters by [83] revealed that LSTs derived from ETM+ at-sensor radiances by ACPC parameters have differences from ground measured LSTs over rice fields within the  $\pm 1.0\text{K}$  range. The sensitivity analysis of the SC algorithm was performed to solve the problem if the accuracy of LST retrieval would be improved after the improving of LSEs estimate. The RMSE of LST is not only affected by the SC coefficient's precision, but also by other factors, which play the main role in the error of LST. These factors are total atmospheric WV content and emissivity. In this study, the method of sensitivity analysis, similarly as in [39, 84] is used. Hence, the contribution to the error of LST is given by Equation. (16).

$$\sigma_{Ts}^{Overall} = \sqrt{\sigma_{alg}^2 + \sigma_{NEAT}^2 + \sigma_{\epsilon}^2 + \sigma_{wv}^2} \quad (16)$$

where  $\sigma_{Ts}^{Overall}$  is the overall standard deviation of LST,  $\sigma_{alg}$  is the standard error of the algorithm,  $\delta_{NEAT}$  is the contribution of the Noise Equivalent Delta Temperature (NEAT),  $\sigma_{\epsilon}$  is the error of LSEs and  $\sigma_{wv}$  is the error of the atmospheric WV content. The  $\sigma_{alg}$  is assessed by [85] and  $\delta_{NEAT}$  of TIRS (@ 280K) is 0.05K for b10 and 0.06K for b11[86] which, errors of LST are negligible. The studies by [77] reported the RMSE values are below 1 K in the SC<sup>Im&S</sup> algorithm when WV contents is between 0.5 and  $2 \text{ g} \cdot \text{cm}^{-2}$ . Therefore, the  $\sigma_{alg}$  is below 1 K since the VW contents of the study area is 1.2 for examined dataset (Table II). In this paper, the sensitivity analysis is carried out on emissivity since emissivity has a serious contribution to the error of the LST. In this regard,  $\sigma_{Ts}$  is given by Equation. (17) for emissivity error.

In the SC algorithm, the atmospheric parameters of the study area given in Table II are used. In addition, the mean surface temperature is set to 300 K and the mean surface emissivity values are computed for band 10 and 11 using Table 1.

$$\sigma_{Ts} = \left( \frac{\partial Ts}{\partial \epsilon} \right) e_{\epsilon} = \frac{T_{sen}^2 \times \left( L^\uparrow + \frac{L^\downarrow}{\tau} - \frac{L_{sen}}{\tau} \right)}{k_2 \times L_{sen} \times \epsilon^2 \times \left( \frac{1}{\lambda_e} + \frac{\lambda_e^4}{k_1} \right)} \times e_{\epsilon} \quad (17)$$

where  $\sigma_{Ts}$  is the standard deviation of LST,  $T_{sen}$  is the at-sensor brightness temperature in K, and  $e_{\epsilon}$  is the error of LSE. The error of LST in Fig. 14 was obtained considering the set parameters in the study area.

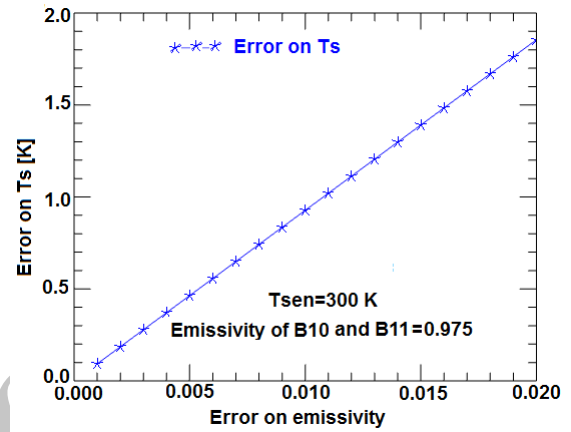


Fig 14. Errors on land surface temperature (Ts) due to the errors on the land surface emissivity

Theoretically, based on the achieved LSEs the LST improvement of the SC algorithm is computed using the error propagation theory. The impact of the LSE improvement on the LST error using the SC algorithm for thermal band 10 and 11 are obtained by Equation. (12). Table (III), shows the impact of the LSE improvement on the LST for the initial and modified SEBAL-based LSE estimation methods.

It is noteworthy that in the sensitivity analysis only the impact of LSE parameter on LST was conducted. As shown in Fig.1, two examined LSE of ASTER product is located in different part of one scene in LDCM data. Since, the first and second LSE of ASTER product located almost in the non-vegetated and vegetated area, respectively, the effect of LAI parameter is ineffective in LSE estimation. As a result, the difference between initial and modified SEBAL-based is less. In contrast, in the first scene of ASTER product is almost located in vegetated area, the impact of the improvement LSE on LST has a noticeable difference (Table III). This difference is the result of the impact of surface parameters such as moisture, texture, canopy of vegetation and so on in the LSE estimation.

**Table III. The impact of the LSE improvement on the LST based on the SC algorithm<sup>a</sup>**

Examined Scenes	Methods	TIRS Bands	RMSE of LSEs	$\sigma_{T_s}$
1st scene	SEBAL	10	1.37 %	1.16 K
	SEBAL	11	1.12 %	1.03 K
	M_SEBAL	10	0.46 %	0.39K
	M_SEBAL	11	0.39 %	0.36K
2nd scene	SEBAL	10	0.69 %	0.60K
	SEBAL	11	0.65 %	0.58K
	M_SEBAL	10	0.46 %	0.40K
	M_SEBAL	11	0.43 %	0.39K

a.  $T_s$ , land surface temperature;  $\sigma_{T_s}$ , root mean square error of  $T_s$

## V. CONCLUSION

In this paper, the effects of SRF and the effective wavelength on SEBAL-based LSE estimation method was investigated. The 8-14  $\mu\text{m}$  spectral domain of initial SEBAL, divided into two very narrowband TIR bands (10.60 - 11.19  $\mu\text{m}$ ) and (11.50 - 12.51  $\mu\text{m}$ ) spectral ranges in the LDCM. This study investigates the effects of SRF and effective wavelength of two LDCM TIR bands on SEBAL-based LSE estimation method. The effectiveness of the proposed  $M_{LSE}$ SEBAL method is empirically evaluated over one scene of LDCM data and the LSEs achieved by initial and modification methods were compared to the LSE product of the ASTER in two cases of IBCV and CBCV. The results obtained by IBCV (Fig. 8a, b, and Fig. 9a, b) showed that in comparison with three common LSE estimation methods, the achieved results by the  $M_{LSE}$ SEBAL method demonstrated better performance in terms of RMSE on both examined ASTER scenes. The RMSE of LSE obtained by  $M_{LSE}$ SEBAL method is 1.59% and 1.21% in thermal band 10 of the first and second examined scenes, respectively. Similarity, for the thermal band 11, the error values are 1.56% and 0.98% in the two examined ASTER scenes, respectively. Moreover, the results (Figures 6 and 7a, b) showed that if there is little difference in the effective wavelength between broadband and narrowband, the LSE estimation is almost identical to the non-vegetated area and there is no significant difference, while it is non-negligible in the vegetated area. In contrast, if there is a relatively large difference between the effective wavelength and SRF between them, areas with vegetation and no vegetation have the greatest difference and the same performance in LSE estimation. In addition, analysis of the results showed that the effect of SRF and wavelengths range of thermal bands in the LSE estimation is not negligible. On average, there are 0.22% and 0.61%

improvement between initial and modified SEBAL methodology for band 10 and band 11, respectively. As previously mentioned a small improvement in LSE can influence LST remarkably. In addition, the obtained results of CBCV (Fig. 12a, b and Fig. 13a, b) showed that in classes that consist density vegetation the  $M_{LSE}$ SEBAL demonstrated almost the better performance rather than the compared LSE estimation methods. These changes may be the result of the impact of environmental parameters such as moisture, texture, the canopy of vegetation and SRF, which can be affected on the LSE estimation.

Moreover, the sensitivity analysis of the SC algorithm was performed to solve the problem if the accuracy of LST retrieval would be improved after the improving of LSEs estimate. The RMSE values of LSE obtained by initial and  $M_{LSE}$ SEBAL methods are 1.37% (for b10) and 1.12% (for b 11) which , lead to 1.16 K and 1.03 K errors and 0.46% (for b10) and 0.39% (for b 11) that lead to 0.39 K and 0.36 K errors in the LST retrieval in the first scene, respectively. Similarly, for the second scene, the RMSE values are 0.69% (for b10) and 0.65% (for b 11) which lead to 0.6 K and 0.58 K errors and 0.46% (for b10) and 0.43% (for b 11) which lead to 0.40 K and 0.39 K errors, respectively. Since, the first and second LSE of ASTER product located almost in the non-vegetated and vegetated area, respectively, the effect of LAI parameter is ineffective in LSE estimation. As a result, the difference between initial and modified SEBAL-based is less. In contrast, in the first scene of ASTER product is almost located in vegetated area, the impact of the improvement LSE on LST has a noticeable difference (Table III). This difference is the result of the impact of surface parameters such as moisture, texture, canopy of vegetation and so on in the LSE estimation.

In sum, since LSE is an important intrinsic property of the materials its accurate estimation with a greater computational cost is valuable. In this regard, according to the experimental results, the modified SEBAL-based LSE estimation method,  $M_{LSE}$ SEBAL, yielded a proper estimation for two datasets, which demonstrated their stability in contrast to the compared methods for LSE estimation and LST retrieval.

## ACKNOWLEDGEMENTS

The authors wish to express their gratitude to any specific product, namely, LDCM imagery held in the USGS archives and reprocessing datasets (landsat.usgs.gov) and the Johns the Jet Propulsion Laboratory (JPL) due to the ASTER spectral library.

## REFERENCE

- [1] Mitraka, Z., et al., Improving the estimation of urban surface emissivity based on sub-pixel classification of high resolution

- satellite imagery. *Remote Sensing of Environment*, 2012. 117: p. 125-134.
- [2] Li, Z.-L., et al., Satellite-derived land surface temperature: Current status and perspectives. *Remote Sensing of Environment*, 2013. 131: p. 14-37.
- [3] Li, Z.-L., et al., Evaluation of six methods for extracting relative emissivity spectra from thermal infrared images. *Remote Sensing of Environment*, 1999. 69(3): p. 197-214.
- [4] Becker, F. and Z.L. Li, Surface temperature and emissivity at various scales: Definition, measurement and related problems. *Remote Sensing Reviews*, 1995. 12(3-4): p. 225-253.
- [5] Tang, B.-H., et al., An improved NDVI-based threshold method for estimating land surface emissivity using MODIS satellite data. *International Journal of Remote Sensing*, 2015(ahead-of-print): p. 1-15.
- [6] Rong, Y., et al. Emissivity measurement for low emissivity objects by two blackbody tube methods. in *IEEE International Geoscience and Remote Sensing Symposium (IGARSS)*. 2012. Munich, Germany, July 22-27.
- [7] Jiang, J.-x., Q.-h. Liu, and H. Li. A modified NDVI threshold method for estimating LSE from FY3A/VIRR data. in *2nd International Conference on Remote Sensing, Environment and Transportation Engineering (RSETE)*. 2012. Nanjing, Jiangsu, China, 01-03 Jun: IEEE.
- [8] Boonmee, M., Land Surface Temperature and Emissivity Retrieval from Thermal Infrared Hyperspectral Imagery. 2007, Rochester Institute of Technology, PHD Thesis.
- [9] Sobrino, J.A., et al., Land surface emissivity retrieval from different VNIR and TIR sensors. *IEEE Transactions on Geoscience and Remote Sensing*, 2008. 46(2): p. 316-327.
- [10] Van de Griend, A. and M. Owe, On the relationship between thermal emissivity and the normalized difference vegetation index for natural surfaces. *International Journal of remote sensing*, 1993. 14(6): p. 1119-1131.
- [11] Bastiaanssen, W., et al., A remote sensing surface energy balance algorithm for land (SEBAL). 1. Formulation. *Journal of hydrology*, 1998. 212: p. 198-212.
- [12] Snyder, W.C., et al., Classification-based emissivity for land surface temperature measurement from space. *International Journal of Remote Sensing*, 1998. 19(14): p. 2753-2774.
- [13] Sun, D. and R.T. Pinker, Estimation of land surface temperature from a Geostationary Operational Environmental Satellite (GOES-8). *Journal of Geophysical Research: Atmospheres (1984–2012)*, 2003. 108(D11).
- [14] Wan, Z. and Z.-L. Li, A physics-based algorithm for retrieving land-surface emissivity and temperature from EOS/MODIS data. *Geoscience and Remote Sensing, IEEE Transactions on*, 1997. 35(4): p. 980-996.
- [15] Realmuto, V. Separating the effects of temperature and emissivity: Emissivity spectrum normalization. in *Proc. 2nd TIMS Workshop*. 1990.
- [16] Coll, C., et al., Adjusted Normalized Emissivity Method for surface temperature and emissivity retrieval from optical and thermal infrared remote sensing data. *Journal of Geophysical Research: Atmospheres (1984–2012)*, 2003. 108(D23).
- [17] Valor, E., et al. The Adjusted Normalized Emissivity Method (ANEM) for land surface temperature and emissivity recovery. in *Geoscience and Remote Sensing Symposium*, 2003. *IGARSS'03. Proceedings*. 2003 IEEE International. 2003. IEEE.
- [18] Richter, R. and D. Schläpfer, Atmospheric/topographic correction for satellite imagery, in *DLR report DLR-IB*. 2014: DLR-German Aerospace Center, Germany.
- [19] Kahle, A.B., D.P. Madura, and J.M. Soha, Middle infrared multispectral aircraft scanner data: Analysis for geological applications. *Applied Optics*, 1980. 19(14): p. 2279-2290.
- [20] Gillespie, A.R., et al., Temperature/emissivity separation algorithm theoretical basis document, version 2.4. ATBD contract NAS5-31372, NASA, 1999.
- [21] Barducci, A. and I. Pippi, Temperature and emissivity retrieval from remotely sensed images using the "grey body emissivity" method. *Geoscience and Remote Sensing, IEEE Transactions on*, 1996. 34(3): p. 681-695.
- [22] Wang, N., et al., Retrieval of atmospheric and land surface parameters from satellite-based thermal infrared hyperspectral data using a neural network technique. *International Journal of Remote Sensing*, 2013. 34(9-10): p. 3485-3502.
- [23] Ma, X.L., et al., Simultaneous retrieval of atmospheric profiles, land-surface temperature, and surface emissivity from Moderate-Resolution Imaging Spectroradiometer thermal infrared data: Extension of a two-step physical algorithm. *Applied optics*, 2002. 41(5): p. 909-924.
- [24] Taylor, S.E., Measured emissivity of soils in the southeast United States. *Remote Sensing of Environment*, 1979. 8(4): p. 359-364.
- [25] Salisbury, J.W. and D.M. D'Aria, Emissivity of terrestrial materials in the 8–14  $\mu\text{m}$  atmospheric window. *Remote Sensing of Environment*, 1992. 42(2): p. 83-106.
- [26] Wang, K., et al., Estimation of surface long wave radiation and broadband emissivity using Moderate Resolution Imaging Spectroradiometer (MODIS) land surface temperature/emissivity products. *Journal of Geophysical Research: Atmospheres (1984–2012)*, 2005. 110(D11).
- [27] Joseph, G., *Fundamentals of remote sensing*. 2005: Universities Press.
- [28] Minacapilli, M., et al., Estimation of actual evapotranspiration of Mediterranean perennial crops by means of remote-sensing based surface energy balance models. *Hydrology and Earth System Sciences*, 2009. 13(7): p. 1061-1074.
- [29] Allen, R., et al., SEBAL (Surface Energy Balance Algorithms for Land). *Advance Training and Users Manual–Idaho Implementation*, version, 2002. 1: p. 97.
- [30] Feizizadeh, B., et al., Monitoring land surface temperature relationship to land use/land cover from satellite imagery in Maraqeh County, Iran. *Journal of Environmental Planning and Management*, 2013. 56(9): p. 1290-1315.
- [31] Reuter, D., et al. The thermal infrared sensor on the landsat data continuity mission. in *Geoscience and Remote Sensing Symposium (IGARSS)*, 2010 IEEE International. 2010. IEEE.
- [32] Ogawa, K., et al., Estimation of broadband land surface emissivity from multi-spectral thermal infrared remote sensing. *Agronomie*, 2002. 22(6): p. 695-696.
- [33] Hulley, G.C., S.J. Hook, and A.M. Baldridge, Validation of the North American ASTER Land Surface Emissivity Database (NAALSED) version 2.0 using pseudo-invariant sand dune sites. *Remote Sensing of Environment*, 2009. 113(10): p. 2224-2233.
- [34] Tang, B.-H., et al., Estimation of broadband surface emissivity from narrowband emissivities. *Optics express*, 2011. 19(1): p. 185-192.
- [35] Wan, Z. and J. Dozier, A generalized split-window algorithm for retrieving land-surface temperature from space. *Geoscience and Remote Sensing, IEEE Transactions on*, 1996. 34(4): p. 892-905.
- [36] Becker, F. and Z.-L. Li, Temperature-independent spectral indices in thermal infrared bands. *Remote Sensing of Environment*, 1990. 32(1): p. 17-33.
- [37] Prata, A., Land surface temperature measurement from space: AATSR algorithm theoretical basis document. Contract Report to ESA, CSIRO Atmospheric Research, Aspendale, Victoria, Australia, 2002. 2002: p. 1-34.
- [38] Hu, H., F. Chen, and Q. Wang. Estimating the effective wavelength of the thermal band for accurate brightness temperature retrieval: methods and comparison. in *Spatial Data Mining and Geographical Knowledge Services (ICSDM)*, 2011 IEEE International Conference on. 2011. IEEE.

- [39] Jiménez-Muñoz, J.C. and J.A. Sobrino, A generalized single-channel method for retrieving land surface temperature from remote sensing data. *Journal of Geophysical Research: Atmospheres* (1984–2012), 2003. 108(D22).
- [40] Irons, J.R., J.L. Dwyer, and J.A. Barsi, The next Landsat satellite: The Landsat data continuity mission. *Remote Sensing of Environment*, 2012. 122: p. 11-21.
- [41] Coll, C., et al., Validation of Landsat-7/ETM+ thermal-band calibration and atmospheric correction with ground-based measurements. *Geoscience and Remote Sensing, IEEE Transactions on*, 2010. 48(1): p. 547-555.
- [42] Salisbury, J.W., A. Wald, and D.M. D'Aria, Thermal-infrared remote sensing and Kirchhoff's law: 1. Laboratory measurements. *Journal of Geophysical Research: Solid Earth* (1978–2012), 1994. 99(B6): p. 11897-11911.
- [43] Korb, A.R., et al., Portable Fourier transform infrared spectroradiometer for field measurements of radiance and emissivity. *Applied Optics*, 1996. 35(10): p. 1679-1692.
- [44] Quan, W., et al., A modified Becker's split-window approach for retrieving land surface temperature from AVHRR and VIRR. *Acta Meteorologica Sinica*, 2012. 26: p. 229-240.
- [45] Baldridge, A., et al., The ASTER spectral library version 2.0. *Remote Sensing of Environment*, 2009. 113(4): p. 711-715.
- [46] Caselles, E., et al., Automatic classification-based generation of thermal infrared land surface emissivity maps using AATSR data over Europe. *Remote Sensing of Environment*, 2012. 124: p. 321-333.
- [47] Sobrino, J.A., J.C. Jiménez-Muñoz, and L. Paolini, Land surface temperature retrieval from LANDSAT TM 5. *Remote Sensing of Environment*, 2004. 90(4): p. 434-440.
- [48] Bhowmick, D., N.A. Hamm, and E.J. Milton, Use of an Airborne Imaging Spectrometer as a Transfer Standard for Atmospheric Correction of SPOT-HRG Data. *Spatial data quality: from process to decisions*, 2009.
- [49] Coll, C., et al., Ground measurements for the validation of land surface temperatures derived from AATSR and MODIS data. *Remote Sensing of Environment*, 2005. 97(3): p. 288-300.
- [50] Zakšek, K., K. Oštir, and Ž. Kokalj, Sky-view factor as a relief visualization technique. *Remote Sensing*, 2011. 3(2): p. 398-415.
- [51] Baret, F., G. Guyot, and D. Major, TSAVI: a vegetation index which minimizes soil brightness effects on LAI and APAR estimation. in *Geoscience and Remote Sensing Symposium, 1989. IGARSS'89. 12th Canadian Symposium on Remote Sensing., 1989 International. 1989. IEEE*.
- [52] Panda, S.S., D.P. Ames, and S. Panigrahi, Application of vegetation indices for agricultural crop yield prediction using neural network techniques. *Remote Sensing*, 2010. 2(3): p. 673-696.
- [53] Qi, J., et al., A modified soil adjusted vegetation index. *Remote sensing of environment*, 1994. 48(2): p. 119-126.
- [54] Feizizadeh, B. and T. Blaschke, Thermal remote sensing for land surface temperature monitoring: Maraqeh County, Iran. in *Geoscience and Remote Sensing Symposium (IGARSS), 2012 IEEE International. 2012. IEEE*.
- [55] Choudhury, B.J., et al., Relations between evaporation coefficients and vegetation indices studied by model simulations. *Remote sensing of environment*, 1994. 50(1): p. 1-17.
- [56] Wang, K. and S. Liang, Evaluation of ASTER and MODIS land surface temperature and emissivity products using long-term surface longwave radiation observations at SURFRAD sites. *Remote Sensing of Environment*, 2009. 113(7): p. 1556-1565.
- [57] Valor, E. and V. Caselles, Mapping land surface emissivity from NDVI: Application to European, African, and South American areas. *Remote sensing of Environment*, 1996. 57(3): p. 167-184.
- [58] Jiménez-Muñoz, J.C., et al., Improved land surface emissivities over agricultural areas using ASTER NDVI. *Remote Sensing of Environment*, 2006. 103(4): p. 474-487.
- [59] Momeni, M. and M. Saradjian, Evaluating NDVI-based emissivities of MODIS bands 31 and 32 using emissivities derived by Day/Night LST algorithm. *Remote Sensing of Environment*, 2007. 106(2): p. 190-198.
- [60] Oltra-Carrió, R., et al., Land surface emissivity retrieval from airborne sensor over urban areas. *Remote Sensing of Environment*, 2012. 123: p. 298-305.
- [61] Walawender, J.P., M.J. Hajto, and P. Iwaniuk, A new ArcGIS toolset for automated mapping of land surface temperature with the use of LANDSAT satellite data. in *Geoscience and Remote Sensing Symposium (IGARSS), 2012 IEEE International. 2012. IEEE*.
- [62] Cristóbal, J., et al., Improvements in land surface temperature retrieval from the Landsat series thermal band using water vapor and air temperature. *Journal of Geophysical Research: Atmospheres* (1984–2012), 2009. 114(D8).
- [63] Jiménez-Muñoz, J., et al. Fractional vegetation cover estimation from PROBA/CHRIS data: Methods, analysis of angular effects and application to the land surface emissivity retrieval. in *Proc. 3rd Workshop CHRIS/Proba. 2005*.
- [64] Li, Z.-L., et al., Land surface emissivity retrieval from satellite data. *International Journal of Remote Sensing*, 2013. 34(9-10): p. 3084-3127.
- [65] Peres, L.F. and C.C. DaCamara, Emissivity maps to retrieve land-surface temperature from MSG/SEVIRI. *Geoscience and Remote Sensing, IEEE Transactions on*, 2005. 43(8): p. 1834-1844.
- [66] Gao, Y. and W. Zhang, LULC classification and topographic correction of Landsat-7 ETM+ imagery in the Yangjia River Watershed: the influence of DEM resolution. *Sensors*, 2009. 9(3): p. 1980-1995.
- [67] Blaschke, T., Object based image analysis for remote sensing. *ISPRS journal of photogrammetry and remote sensing*, 2010. 65(1): p. 2-16.
- [68] Martínez, L., et al. Improvement of the thermal emissivity calculated with the vegetation cover method by using optical atmospherically corrected images. in *Geoscience and Remote Sensing Symposium, 2007. IGARSS 2007. IEEE International. 2007. IEEE*.
- [69] Tang, H. and Z.-L. Li, *Future Development and Perspectives, in Quantitative Remote Sensing in Thermal Infrared. 2014, Springer. p. 257-279*.
- [70] Yu, X., X. Guo, and Z. Wu, Land Surface Temperature Retrieval from Landsat 8 TIRS—Comparison between Radiative Transfer Equation-Based Method, Split Window Algorithm and Single Channel Method. *Remote Sensing*, 2014. 6(10): p. 9829-9852.
- [71] Weng, Q. and P. Fu, Modeling annual parameters of clear-sky land surface temperature variations and evaluating the impact of cloud cover using time series of Landsat TIR data. *Remote Sensing of Environment*, 2014. 140: p. 267-278.
- [72] Weng, Q., P. Fu, and F. Gao, Generating daily land surface temperature at Landsat resolution by fusing Landsat and MODIS data. *Remote Sensing of Environment*, 2014. 145: p. 55-67.
- [73] Roy, D.P., et al., Landsat-8: Science and product vision for terrestrial global change research. *RS of Environment*, 2014. 145: p. 154-172.
- [74] Cook, M., et al., Development of an operational calibration methodology for the Landsat thermal data archive and initial testing of the atmospheric compensation component of a Land Surface Temperature (LST) Product from the archive. *Remote Sensing*, 2014. 6(11): p. 11244-11266.
- [75] Markham, B.L., et al., Landsat sensor performance: history and current status. *IEEE Transactions on Geoscience and Remote Sensing*, 2004. 42(12): p. 2691-2694.
- [76] Huang, C., et al., An automated approach for reconstructing recent forest disturbance history using dense Landsat time series stacks. *Remote Sensing of Environment*, 2010. 114(1): p. 183-198.
- [77] Jiménez-Muñoz, J.C., et al., Revision of the single-channel algorithm for land surface temperature retrieval from Landsat

- thermal-infrared data. *IEEE Transactions on Geoscience and Remote Sensing*, 2009. 47(1): p. 339-349.
- [78] Qin, Z.-h., A. Karnieli, and P. Berliner, A mono-window algorithm for retrieving land surface temperature from Landsat TM data and its application to the Israel-Egypt border region. *International Journal of Remote Sensing*, 2001. 22(18): p. 3719-3746.
- [79] Jimenez-Munoz, J.C., et al., Land surface temperature retrieval methods from Landsat-8 thermal infrared sensor data. *Geoscience and Remote Sensing Letters, IEEE*, 2014. 11(10): p. 1840-1843.
- [80] Du, C., et al., A practical split-window algorithm for estimating land surface temperature from Landsat 8 data. *Remote Sensing*, 2015. 7(1): p. 647-665.
- [81] Barsi, J.A., et al. Validation of a web-based atmospheric correction tool for single thermal band instruments. in *Optics & Photonics 2005*. 2005. International Society for Optics and Photonics.
- [82] Barsi, J., J.L. Barker, and J.R. Schott. An atmospheric correction parameter calculator for a single thermal band earth-sensing instrument. in *IEEE International Geoscience and Remote Sensing Symposium, 2003. IGARSS'03. Proceedings. 2003*. IEEE.
- [83] Coll, C., et al., Validation of Landsat-7/ETM+ thermal-band calibration and atmospheric correction with ground-based measurements. *IEEE Transactions on Geoscience and Remote Sensing*, 2010. 48(1): p. 547-555.
- [84] Tang, B.-H., et al., Estimation and validation of land surface temperatures from Chinese second-generation polar-orbit FY-3A VIRR data. *Remote Sensing*, 2015. 7(3): p. 3250-3273.
- [85] Jiménez-Muñoz, J.C., et al., Land Surface Temperature Retrieval Methods From Landsat-8 Thermal Infrared Sensor Data. *Geoscience and Remote Sensing Letters, IEEE*, 2014. 99: p. 1-4.
- [86] Barsi, J.A., et al., Landsat-8 Thermal Infrared Sensor (TIRS) Vicarious Radiometric Calibration. *Remote Sensing*, 2014. 6(11): p. 11607-11626.

Archive of SID